Supplementary Information: Extraordinary Fluorescence from Few Nanoplatelets in Gap Plasmons

Deepshikha Arora[#,1], Nhung Vu Cam[#,1], Wenjie Zhou[#,2], Emek Goksu Durmusoglu[3], Syed Akhil[3], Shijia Cheng[3], Thu Ha Do[4], Golnoush Zamiri[1], Emmanuel Lassalle[4], Xiao Liang[3], Ha Son Tung[4], N. Asger Mortensen[5], Lin Wu[2,*], Hilmi Volkan Demir[3,5,*], Joel K. W. Yang[1,*]

[1]*Engineering Product Development, Singapore University of Technology and Design, Singapore 487372, Singapore.*

[2]*Science, Mathematics and Technology, Singapore University of Technology and Design, Singapore 487372, Singapore.*

[3]*LUMINOUS! Center of Excellence for Semiconductor Lighting and Displays, The Photonics Institute, School of Electrical and Electronic Engineering, School of Physical and Mathematical Sciences, School of Materials Science and Engineering, Nanyang Technological University, Singapore 639798, Singapore.*

[4]*Institute of Materials Research and Engineering (IMRE), Agency for Science, Technology and Research (A*STAR), 2 Fusionopolis Way, Innovis #08-03, Singapore 138634, Republic of Singapore Nanyang Technological University, Singapore 637371, Singapore.*

[5]*POLIMA-Center for Polariton-driven Light-Matter Interactions and Danish Institute for Advanced Study, University of Southern Denmark, DK-5230 Odense M, Denmark*

[6]*UNAM-Institute of Materials Science and Nanotechnology, The National Nanotechnology Research Center, Department of Electrical and Electronics Engineering, Department of Physics, Bilkent University, Bilkent, Ankara, 06800, Turkey.*

Correspondence and requests for materials should be addressed to Lin Wu (email: lin_wu@sutd.edu.sg), Hilmi Volkan Demir (email: hv.demir@ntu.edu.sg) and Joel K. W. Yang (email: joel_yang@sutd.edu.sg)

[#] *These authors made equal contribution to this work.*

S1. Materials and Methods

Cadmium nitrate tetrahydrate ($Cd(NO_3)_2 \cdot 4H_2O$, 99.997%, trace metals basis), sodium myristate (99%), cadmium acetate dihydrate ($Cd(OAc)_2 \cdot 2H_2O$, 98%), selenium (Se, 99.99%, trace metals basis), zinc acetate ($Zn(OAc)_2$, 99.99%, trace metals basis), 1-octanethiol (98.5%), 1-octadecene (ODE, technical-grade), oleic acid (OA, 90%), and oleylamine (OAm, 70%), were purchased from Sigma-Aldrich. Methanol, hexane, toluene, and ethanol were obtained from Merck Millipore and used without any further purification.

Synthesis of Cadmium Myristate

Cadmium myristate ($Cd(Myr)_2$) was synthesized according to the previous methods in the literature.[1] In a typical synthesis, cadmium nitrate tetrahydrate of 1.23 g and sodium myristate of 3.13 g were dissolved in 40 and 250 mL of methanol, respectively. After both the chemicals had completely dissolved, the solutions were mixed and stirred for 1 hour, which resulted in the $Cd(Myr)_2$ white precipitate. The white precipitate was centrifuged, redispersed in methanol, and washed to remove the unreacted precursors or impurities, and the same steps were repeated thrice. Finally, the residue was kept under a vacuum overnight at 50 °C and the completely dried white powder was ground and used further.

Synthesis of 4 Monolayer (ML) CdSe Core Nanoplatelets (NPLs)

Synthesis of the CdSe 4ML core NPLs procedure was adopted from our previously reported protocol with slight modifications.[2] First, in a 50 mL round-bottomed flask 170 mg of $Cd(Myr)_2$ and 12 mg of Selenium in 15 mL of ODE were taken and degassed for 1 hour at 95 °C. Then under N_2 gas temperature was set to 240 °C. At approximately 198 °C where the color of the solution changes to an orangish color, 80 mg of $Cd(OAc)_2 \cdot 2H_2O$ was swiftly added. The reaction mixture was kept at 240 °C for 10 minutes the reaction was quenched with a water bath and cooled to room temperature. The growth was terminated by adding 1 mL of OA at 150 °C and 10 mL of hexane at 60 °C. The resulting 4 ML core CdSe NPLs were precipitated by adding 5 mL of ethanol as antisolvent and centrifuged at 4000 rpm for 10 minutes. Using the size-selective precipitation, the monodispersed 4 ML core CdSe NPLs were achieved and redispersed in hexane and stored for further use.

Synthesis of CdSe/CdZnS Core/shell NPLs

Synthesis of CdSe/CdZnS core/shell NPLs was adopted from the previous report from our group with few modifications.[2] In a 50 mL three-neck round-bottomed flask, 0.1 mmol (26.5 mg) of $Cd(OAc)_2 \cdot 2H_2O$, 0.3 mmol (55 mg) of $Zn(OAc)_2$, 1 mL of OA, and 10 mL of ODE were degassed for 30 minutes at 100 °C. Later the temperature was increased to 200 °C by switching the atmosphere to N_2 gas and maintained for 30 minutes and the solution was clear. The temperature was decreased to 60 °C and 1 mL of 4ML CdSe Core NPLs (having optical density: 2 at 350 nm for 100 μL core NPLs in 3 mL of hexane) were introduced. The solution mixture was degassed for 45 minutes to remove the hexane residuals. After that, N_2 gas was purged in the flask, and the

temperature was set at 300 °C and 1mL of OAm was added at 90 °C. 4 mL of 0.1 M octanethiol (in ODE) was used as an S-source which starts injecting at 165 °C with a syringe pump at 10 mL/h and after 240 °C the injection rate was decreased to 5 mL/h. After completion of the injection, the reaction mixture was kept for another 45 minutes for annealing to complete the shell growth. The reaction was quenched using a water bath and at 60 °C 10 mL hexane was added. The NPLs were washed twice using ethanol as an antisolvent, centrifuged at 6000 rpm for 5 minutes, and redispersed in 5 mL hexane for further use.

Self-assembly of CdSe/CdZnS core/shell NPLs monolayer

We improved the liquid-air interface self-assembly method previously developed by our group to create monolayer films.[3,4] In this process, a substrate was placed into an 8 mm diameter Teflon container filled with acetonitrile (ACN) subphase. Subsequently, a 10 μL hexane solution of NPLs was dropped onto the ACN from the edge of the container. Upon contact with the ACN, the NPLs dispersed across the surface of the subphase. After the hexane evaporated, a uniform, face-down NPLs film was obtained on top of the subphase. To transfer this film onto the substrate, a peristaltic pump was used to remove the ACN from the bottom of the container, allowing the film to settle onto the substrate. Note that to achieve a uniform film, the height of the ACN above the substrate should be as low as possible to minimize movement of the assembled film during drainage. Additionally, we used a silicone oil surfactant to compress the monolayer film further, preventing cracks and voids due to capillary forces from the container walls during deposition.

Characterization methods for colloidal NPLs

Optical Characterization

Absorbance measurements of the NPLs were recorded using the Shimadzu UV-1800 spectrophotometer and PL measurements were recorded by a Shimadzu RF- 5301 PC Spectrofluorophotometer. Our PL-QY measurement setup was equipped with an Ocean Optics S4000 spectrometer, and an integrating sphere was used. For the PL-QY measurements, a clean glass substrate was used for reference, and NPLs solutions were excited at a wavelength of 405 nm (Cobolt Laser).

Transmission electron microscope (TEM)

A single drop of diluted NPLs solution is drop casted on top of a copper grid covered with an amorphous carbon film. The TEM images of the NPLs were obtained using a JEOL 2100F TEM at 200 KV.

Atomic Force Microscopy (AFM)

To confirm the self-assembled NPLs monolayer thin film AFM measurement was performed using the scan-assist mode with 512 resolutions by a Bruker Dimension Icon scanning probe microscope (Bruker 18 Co., Germany).

Scanning Electron Microscope (SEM)

SEM images were obtained using a JSM-7600F (JEOL) instrument at an accelerating voltage of 2 kV in secondary electron detection mode.

Thermogravimetric Analysis (TGA)

TGA analysis was performed using an SDT Q600 instrument under ambient conditions with a powder sample.

S2. Simulation Methods

In this section, we detail the derivation of how the three QNMs (G, A, and D modes) are identified and how their coupling rates are extracted from the scattering cross-section (SCS). We begin with full-wave simulations and establish the connection between classical and quantum models through QNM analysis and a non-Hermitian scattering framework.

Full-wave simulation

Full-wave simulations solving the three-dimensional Maxwell's equations are performed using the finite element method (FEM) within COMSOL Multiphysics (RF module).

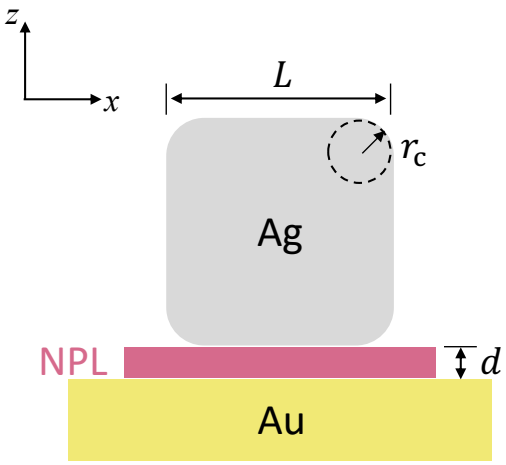

Figure S1: Geometry of the NPoM used in full-wave simulations.

The geometry of the NPoM used in the full-wave simulations is shown in Fig. S1. The cube has a side length of $L = 75$ nm and a corner radius of $r_c = 5$ nm. The gap thickness is set to $d = 7$

nm and is filled by the NPL, which is modeled as a lossless dielectric with a constant refractive index of $n = 1.952$. The permittivity of silver is modeled using the Drude model:

$$\varepsilon(\omega) = \varepsilon_{,\infty}\left(1 - \frac{\omega_p^2}{\omega^2 + i\omega\Gamma}\right), \tag{S1}$$

where $\varepsilon_{,\infty} = 1$, $\omega_p = 1.37 \times 10^{16}$ rad/s, and $\Gamma = 0.0023\omega_p$ [5], and the permittivity of gold is described by a Drude-Lorentz model:

$$\varepsilon(\omega) = \varepsilon_{,\infty}\left(1 - \frac{\omega_{p,1}^2}{\omega^2 - \omega_{0,1}^2 + i\omega\Gamma_1} - \frac{\omega_{p,2}^2}{\omega^2 - \omega_{0,2}^2 + i\omega\Gamma_2}\right), \tag{S2}$$

with parameters: $\varepsilon_{,\infty} = 6$, $\omega_{p,1} = 5.37 \times 10^{15}$ rad/s, $\omega_{0,1} = 0$ and $\Gamma_1 = 6.22 \times 10^{13}$ rad/s; $\omega_{p,2} = 2.26 \times 10^{15}$ rad/s, $\omega_{0,2} = 4.57 \times 10^{15}$ rad/s and $\Gamma_2 = 1.33 \times 10^{15}$ rad/s. The surrounding vacuum is treated as a lossless medium with a constant refractive index of $n = 1$.

To model the scattering, the NPoM structure is excited by a plane wave representing white light, with electric field components in the ratio $E_x : E_y : E_z = 1 : 1 : \sqrt{2}$ and an amplitude of $|E_0| = 1$ V/m. This configuration effectively excites bright QNMs with radiative decay channels—such as the A and G modes—within the energy range of 1.50—2.25 eV. A Perfectly Matched Layer (PML) boundary condition is applied to suppress back reflections. The scattering power P_{sc} is obtained by integrating the power flux around the scatterer, and the scattering cross-section (SCS) is calculated using $P_{\text{sc}}/I_{\text{inc}} = P_{\text{sc}} \cdot (2Z)/|E_0|^2$, where I_{inc} represents the intensity of the incident wave and $Z = \sqrt{\mu\mu_0/(\varepsilon\varepsilon_0)}$ is the impedance of the medium. Note that tunneling effects [6] and nonlocal effects [7] are neglected throughout the simulations.

To model the PL, we use the same geometric configuration as in the scattering simulations. Instead of a plane wave, the PL is simulated as the emission from an excited quantum emitter (QE)

positioned at the corner of the gap region (as shown in the inset of Fig. 3(a)). An electric dipole source is introduced, oscillating in the in-plane direction with component ratios $|\vec{\mu}_x| : |\vec{\mu}_y| = 1 : 1$. The dipole moment is set to $\mu = 4.8 \times 10^{-29}$ C·m, based on experimental measurements. The PL signal is obtained by integrating the radiated power flux in the far-field surrounding the NPoM.

Quasinormal modes analysis

Quasinormal modes (QNMs) are the intrinsic resonant modes of a system, defined without the need for external excitation [5]. In nonmagnetic systems, QNMs are obtained by solving the eigenvalue problem of the time-harmonic, source-free Maxwell's equations:

$$\begin{bmatrix} 0 & -i\mu_0^{-1}\nabla\times \\ i\varepsilon(\widetilde{\omega}_j) & 0 \end{bmatrix} \begin{bmatrix} \widetilde{\mathbf{H}}_j \\ \widetilde{\mathbf{E}}_j \end{bmatrix} = \widetilde{\omega}_j \begin{bmatrix} \widetilde{\mathbf{H}}_j \\ \widetilde{\mathbf{E}}_j \end{bmatrix}, \tag{S3}$$

where $\varepsilon(\widetilde{\omega}_j)$ is the permittivity, μ_0 is the vacuum permeability, and $\widetilde{\mathbf{H}}_j$, $\widetilde{\mathbf{E}}_j$ are the QNMs' electric and magnetic fields, satisfying the Sommerfeld outgoing-wave conditions. For dispersive materials like silver and gold, this eigenvalue problem becomes nonlinear due to the frequency dependence of permittivity. To simplify it, we use the Drude model for silver and the Drude–Lorentz model for gold—consistent with our full-wave simulations.

The Drude-Lorentz poles introduce two hidden auxiliary fields to account for the intraband transitions of free electrons:

$$\widetilde{\mathbf{P}} = \left(\varepsilon_{(Au)}(\omega) - \varepsilon_{(Au),\infty}\right)\widetilde{\mathbf{E}} \tag{S4}$$

$$\widetilde{\mathbf{J}} = -i\omega\widetilde{\mathbf{P}}. \tag{S5}$$

Here, $\widetilde{\mathbf{P}}$ and $\widetilde{\mathbf{J}}$ represent the auxiliary polarization and electric current, respectively. The eigenvectors are now expanded to $\widetilde{\psi}_j = \left[\widetilde{\mathbf{H}}_j, \widetilde{\mathbf{E}}_j, \widetilde{\mathbf{P}}_j, \widetilde{\mathbf{J}}_j\right]^{\mathbf{T}}$, and the system becomes a linear eigenproblem:

$$\widetilde{H}\widetilde{\psi}_j = \begin{bmatrix} 0 & -i\mu_0^{-1}\nabla\times & 0 & 0 \\ i\varepsilon_\infty^{-1}\nabla\times & 0 & 0 & -i\varepsilon_\infty^{-1} \\ 0 & 0 & 0 & i \\ 0 & i\omega_p^2\varepsilon_\infty & 0 & -i\Gamma \end{bmatrix} \widetilde{\psi}_j = \widetilde{\omega}_j\widetilde{\psi}_j. \tag{S6}$$

To compute the QNMs of the NPoM, we use COMSOL to define the structure and material parameters, consistent with our full-wave simulation settings. Then, we employ the open-source modal analysis toolbox "MAN" [8], integrated with MATLAB and COMSOL Multiphysics (RF module), to determine the characteristics of the QNMs [9].

Non-Hermitian scattering model

In a scattering problem involving n quasi-normal modes (QNMs), where $n \geq 2$, the total Hamiltonian is described as $\hat{H} = \hat{H}_0 + \hat{V}$. Here, $\hat{H}_0$ corresponds to the free Hamiltonian, while $\hat{V}$ represents the interaction potential. Both $\hat{H}_0$ and $\hat{V}$ are formulated using Fock states, and are expressed as follows:

$$\hat{H}_0 = \sum_j^n \hbar\omega_j a_j^\dagger a_j + \sum_l \hbar\omega_l B_l^{\mathrm{r}\dagger} B_l^{\mathrm{r}} + \sum_m \hbar\omega_m D_m^{\mathrm{nr}\dagger} D_m^{\mathrm{nr}}, \tag{S7}$$

$$\hat{V} = \sum_j^n \sum_k^n \hbar g_{jk}(a_j^\dagger a_k + a_k^\dagger a_j) \tag{S8}$$

$$+ \sum_j^n \sum_l \hbar V_{jl}(B_l^{\mathrm{r}\dagger} a_j + a_j^\dagger B_l^{\mathrm{r}}) + \sum_j^n \sum_m \hbar V_{jm}(D_m^{\mathrm{nr}\dagger} a_j + a_j^\dagger D_m^{\mathrm{nr}}). \tag{S9}$$

Here, a_j (or $a_j^\dagger$) represents the annihilation (or creation) operator for the j^{th} mode with resonance energy $\hbar\omega_j$. Similarly, the vacuum and thermal reservoirs are quantized in terms of Fock states, denoted by integers l and m, which correspond to the system's radiative and non-radiative decay channels, respectively. The operators B_l^{r} (or $B_l^{\text{r}\dagger}$) and D_m^{nr} (or $D_m^{\text{nr}\dagger}$) represent the annihilation (or creation) operators for the l^{th} and m^{th} states.

The first term in $\hat{V}$ describes the near-field coupling between a_j and a_k, where $j \neq k$, with the interaction characterized by the coupling rate g_{jk}; note that $g_{jk} = 0$ when $j = k$. The second and third terms account for energy leakage through coupling to the vacuum and thermal reservoirs, governed by the channel coefficients V_{jl}^{r} and V_{jm}^{nr} [10].

According to Fermi's golden rule, the scattering cross section (SCS) is determined by calculating the transition rate between the system's initial (i) and final (f) states. This process involves evaluating the matrix element of the interaction responsible for the transition and integrating over the density of final states, which accounts for the number and distribution of possible final states. The SCS is expressed as:

$$\sigma_{\text{sc}} = \frac{\sum_{i,f} W_{i\to f}}{\phi} = \frac{2\pi}{\hbar\phi}\sum_{i,f}|\mathcal{T}_{i\to f}|^2\delta(E_f - E_i), \tag{S10}$$

where $\mathcal{T}_{i\to f}$ represents the transition matrix element, which is crucial in determining the SCS. This matrix element is formulated as the product of three components, each enclosed in square brackets:

$$\mathcal{T}_{i\to f} = \langle f|\hat{V}^\dagger\hat{P}^\dagger\hat{G}(\widetilde{\omega})\hat{P}\hat{V}|i\rangle = \sum_{j,k}^{n}[\langle f|\hat{V}^\dagger|\mathbf{1}_j^a\rangle][\langle\mathbf{1}_j^a|\hat{G}(\widetilde{\omega})|\mathbf{1}_k^a\rangle][\langle\mathbf{1}_k^a|\hat{V}|i\rangle]. \tag{S11}$$

Here, the dyadic $\hat{P} = \sum_j^n|\mathbf{1}_j^a\rangle\langle\mathbf{1}_j^a|$ is established within the system's Hilbert space to facilitate the

connection between the input vector $\hat{V}|i\rangle$ and the conjugate of the output vector $[\hat{V}|f\rangle]^\dagger$ via the system's Green's function $\hat{G}(\widetilde{\omega})$.

Following Ref.[10], the transition matrix $\mathcal{T}_{i\to f}$ is given by:

$$\begin{aligned}\mathcal{T}_{i\to f} &= \sum_{j,k}^{n}[\langle f|\hat{V}|\mathbf{1}_j^a\rangle]\cdot[\frac{1}{\langle\mathbf{1}_j^a|\widetilde{\omega}|\mathbf{1}_k^a\rangle-\langle\mathbf{1}_j^a|\hat{H}_0|\mathbf{1}_k^a\rangle-\langle\mathbf{1}_j^a|\hat{V}|\mathbf{1}_k^a\rangle}]\cdot[\langle\mathbf{1}_k^a|\hat{V}|i\rangle] \\ &= \begin{bmatrix}V_1^{\mathrm{r}} & \cdots & V_n^{\mathrm{r}}\end{bmatrix}\cdot\begin{bmatrix}\widetilde{\omega}-\omega_1+\frac{i}{2}(\gamma_1^{\mathrm{r}}+\gamma_1^{\mathrm{nr}}) & \cdots & -g_{1n}+\frac{i}{2}\sqrt{\gamma_1^{\mathrm{r}}\gamma_n^{\mathrm{r}}} \\ \vdots & \ddots & \vdots \\ -g_{n1}+\frac{i}{2}\sqrt{\gamma_n^{\mathrm{r}}\gamma_1^{\mathrm{r}}} & \cdots & \widetilde{\omega}-\omega_n+\frac{i}{2}(\gamma_n^{\mathrm{r}}+\gamma_n^{\mathrm{nr}})\end{bmatrix}^{-1}\cdot\begin{bmatrix}V_1^{\mathrm{r}} \\ \vdots \\ V_n^{\mathrm{r}}\end{bmatrix}.\end{aligned} \tag{S12}$$

We now examine a straightforward single-mode scattering process to extract V_j^r, focusing on a QNM characterized by the complex frequency $\omega_0 - i\gamma_0^{\mathrm{t}}$. The SCS for this single-mode is calculated given by:

$$\sigma_0(\omega) = \frac{1}{(\omega-\omega_0)^2+(\gamma_0^{\mathrm{t}}/2)^2}\cdot\frac{2\pi}{\phi}\sum_{i,f}|V_0^{\mathrm{r}}\cdot V_0^{\mathrm{r}}|^2\delta(E_f-E_i) \tag{S13}$$

$$= \frac{1}{(\omega-\omega_0)^2+(\gamma_0^{\mathrm{t}}/2)^2}\cdot\frac{2\pi}{\phi}\int d\Omega dk_f\left(\frac{L_0}{2\pi}\right)^3 k_f^2\left[\frac{\mu_0^{\mathrm{r}}\mu_0^{\mathrm{r}}\omega_0^2}{2\varepsilon_0\sqrt{\omega_f\omega_i}\mathcal{V}_0}\right]^2[(\vec{e}_0\cdot\vec{e}_f)(\vec{e}_0\cdot\vec{e}_i)]^2\delta(\omega_f-\omega_i). \tag{S14}$$

For a single photon, the radiative flux density can be expressed as $\phi = c/L_0^3$. Assuming ideal alignment where the modal field vector $\vec{e}_0$ perfectly aligns with the excitation field vector $\vec{e}_i$ such that $\vec{e}_0\cdot\vec{e}_i = 1$, the SCS simplifies accordingly:

$$\sigma_0(\omega) = \frac{1}{(\omega-\omega_0)^2+(\gamma_0^{\mathrm{t}}/2)^2}\cdot\frac{1}{4\pi^2 c}\frac{(\mu_0^{\mathrm{r}}\mu_0^{\mathrm{r}}\omega_0^2)^2}{4\varepsilon_0^2}\int d\Omega(\vec{e}_0\cdot\vec{e}_f)^2 dk_f\frac{k_f^2}{\omega_f^2} \tag{S15}$$

$$= \frac{1}{(\omega-\omega_0)^2+(\gamma_0^{\mathrm{t}}/2)^2}\cdot\frac{(\mu_0^{\mathrm{r}}\mu_0^{\mathrm{r}}\omega_0^2)^2}{16\pi^2\varepsilon_0^2 c^3}\frac{8\pi}{3} \tag{S16}$$

Since the spontaneous radiative decay rate in a vacuum is given by $\gamma_0^r = \omega_0^3(\mu_0^r)^2/(3\pi c^3\varepsilon_0)$, we can substitute $(\omega_0\mu_0^r)^2 = 3\pi c^3\varepsilon_0\gamma_0^r/\omega_0$ into Eq. (S16):

$$\sigma_0(\omega) = \frac{3}{2\pi}\frac{1}{(\omega-\omega_0)^2+(\gamma_0^t/2)^2}\cdot\left(\frac{\lambda_0\gamma_0^r}{2}\right)^2 \tag{S17}$$

$$= \frac{3}{2\pi}\left|\sqrt{\frac{\lambda_0\gamma_0^r}{2}}\frac{1}{\omega-\omega_0+i\gamma_0^t/2}\sqrt{\frac{\lambda_0\gamma_0^r}{2}}\right|^2, \tag{S18}$$

where λ_0 represents the wavelength associated with ω_0, and $\sqrt{\lambda_0\gamma_0^r/2}$ is identified as the dressed channel coefficient, which is derived from V_0^r.

Expanding this approach to encompass scattering processes involving any number of QNMs, the SCS is generalized and expressed as follows:

$$\sigma_{sc}(\omega) = \frac{3}{2\pi}\left|\begin{bmatrix}\sqrt{\frac{\lambda_1\gamma_1^r}{2}}\\ \vdots \\ \sqrt{\frac{\lambda_n\gamma_n^r}{2}}\end{bmatrix}^T\cdot\begin{bmatrix}\widetilde{\omega}-\omega_1+\frac{i}{2}(\gamma_1^r+\gamma_1^{nr}) & \cdots & -g_{1n}+\frac{i}{2}\sqrt{\gamma_1^r\gamma_n^r}\\ \vdots & \ddots & \vdots \\ -g_{n1}+\frac{i}{2}\sqrt{\gamma_n^r\gamma_1^r} & \cdots & \widetilde{\omega}-\omega_n+\frac{i}{2}(\gamma_n^r+\gamma_n^{nr})\end{bmatrix}^{-1}\cdot\begin{bmatrix}\sqrt{\frac{\lambda_1\gamma_1^r}{2}}\\ \vdots \\ \sqrt{\frac{\lambda_n\gamma_n^r}{2}}\end{bmatrix}\right|^2. \tag{S19}$$

Hence, we fit the SCS with the black dashed line in **Fig. 3(c)** by:

$$\sigma_{sc}(\widetilde{\omega}) =$$

$$\frac{3}{2\pi}\left|\begin{bmatrix}\sqrt{\frac{\lambda_\alpha\gamma_\alpha^r}{2}}\\ \sqrt{\frac{\lambda_{\beta_1}\gamma_{\beta_1}^r}{2}}\\ \sqrt{\frac{\lambda_{\beta_2}\gamma_{\beta_2}^r}{2}}\end{bmatrix}^T\cdot\begin{bmatrix}\widetilde{\omega}-\omega_\alpha+\frac{i}{2}(\gamma_\alpha^r+\gamma_\alpha^{nr}) & -g_{\alpha\beta_1}+\frac{i}{2}\sqrt{\gamma_\alpha^r\gamma_{\beta_1}^r} & -g_{\alpha\beta_2}+\frac{i}{2}\sqrt{\gamma_\alpha^r\gamma_{\beta_2}^r}\\ -g_{\alpha\beta_1}+\frac{i}{2}\sqrt{\gamma_{\beta_1}^r\gamma_\alpha^r} & \widetilde{\omega}-\omega_{\beta_1}+\frac{i}{2}(\gamma_{\beta_1}^r+\gamma_{\beta_1}^{nr}) & -g_{\beta_1\beta_2}+\frac{i}{2}\sqrt{\gamma_{\beta_1}^r\gamma_{\beta_2}^r}\\ -g_{\alpha\beta_2}+\frac{i}{2}\sqrt{\gamma_{\beta_2}^r\gamma_\alpha^r} & -g_{\beta_1\beta_2}+\frac{i}{2}\sqrt{\gamma_{\beta_2}^r\gamma_{\beta_1}^r} & \widetilde{\omega}-\omega_{\beta_2}+\frac{i}{2}(\gamma_{\beta_2}^r+\gamma_{\beta_2}^{nr})\end{bmatrix}^{-1}\cdot\begin{bmatrix}\sqrt{\frac{\lambda_\alpha\gamma_\alpha^r}{2}}\\ \sqrt{\frac{\lambda_{\beta_1}\gamma_{\beta_1}^r}{2}}\\ \sqrt{\frac{\lambda_{\beta_2}\gamma_{\beta_2}^r}{2}}\end{bmatrix}\right|^2. \tag{S20}$$

S3. Additional Figures

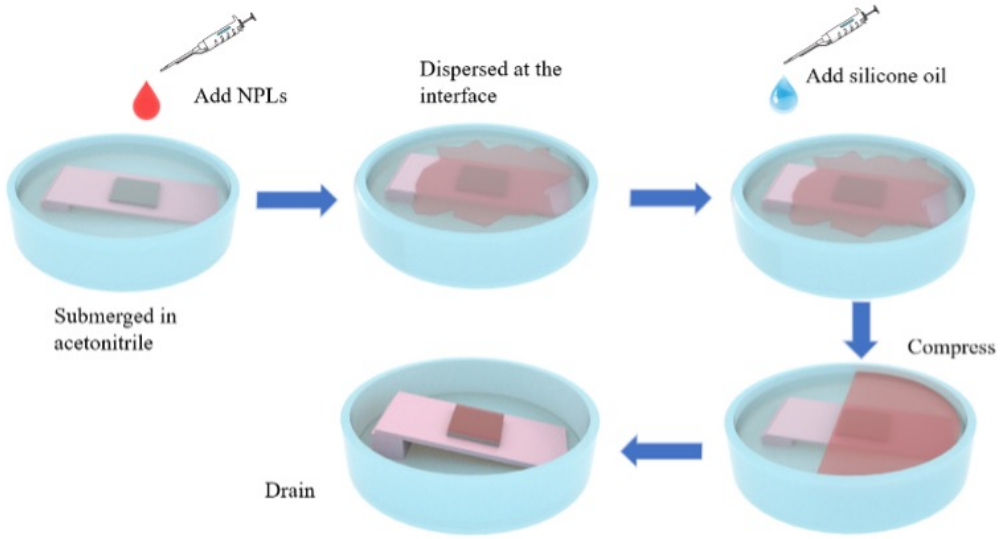

Figure S2: Schematic illustration of the liquid-air interface self-assembly process used for NPL monolayer deposition.

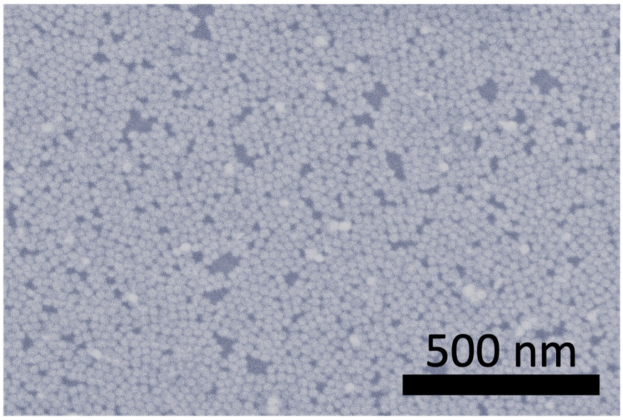

Figure S3: Scanning Electron Microscope (SEM) image of deposited NPL monolayer showing NPLs lying flat on the substrate. The few brighter regions indicate regions where NPLs are overlapping with one another.

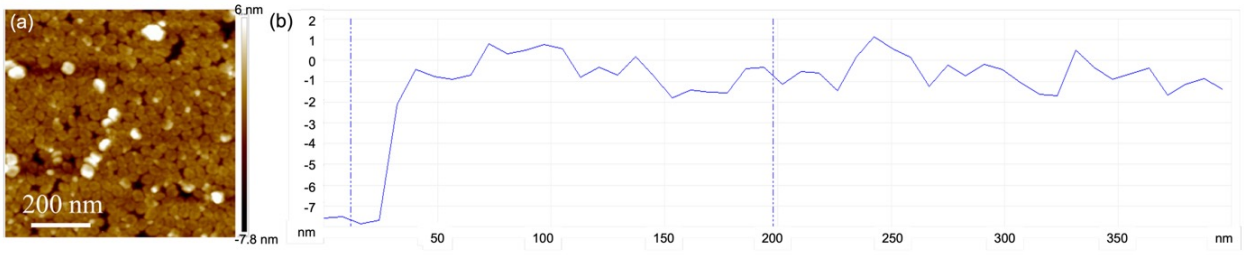

Figure S4: Topography of the surface of the monolayer NPL film taken via atomic force microscopy (AFM). (b) Film thickness and roughness measurement for a monolayer of NPL.

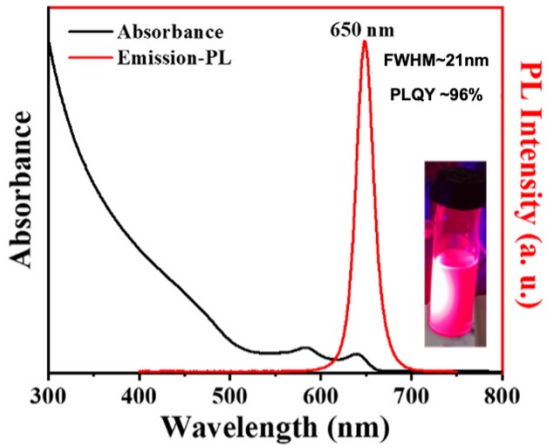

Figure S5: Absorbance (black line) and PL emission spectra (red line). Inset: NPL colloidal solution under UV excitation.

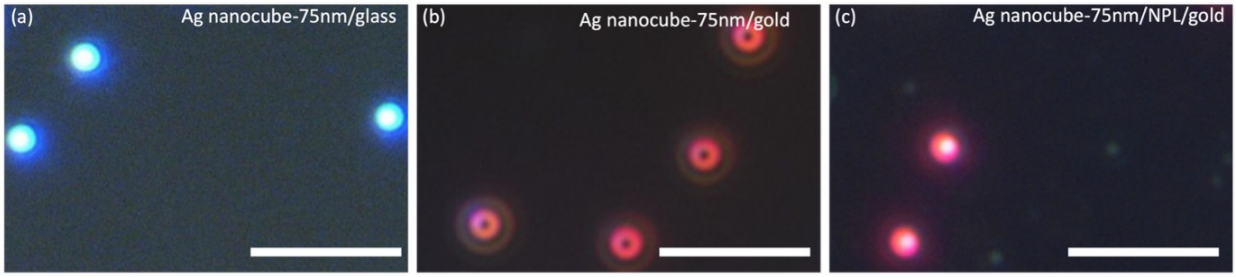

Figure S6: White light dark field scattering image of 75 nm Ag NC on (a) low refractive index glass substrate appear blue (b) template stripped gold substrate appear as donuts/ ring like structures due to the anisotropic scattering because of plasmon coupling. (c) template stripped gold substrate with NPL monolayer as the spacer, the scattered light appears as solid red dots. The scale bar is 10 um.

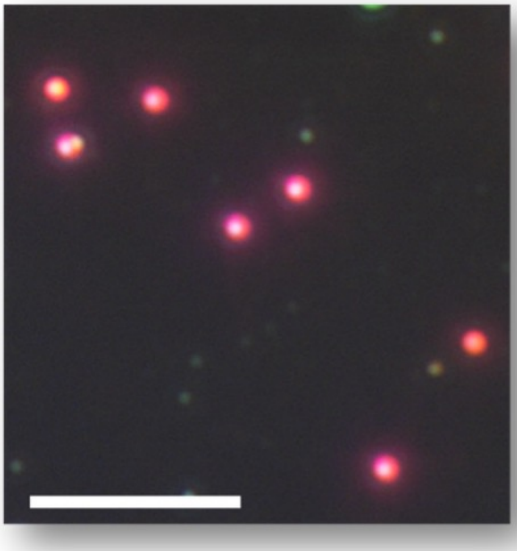

Figure S7: Fluorescence image under laser excitation at 405 nm of 75 nm Ag NC on gold substrate with core-shell NPL monolayer in between. The scale bar is 10um.

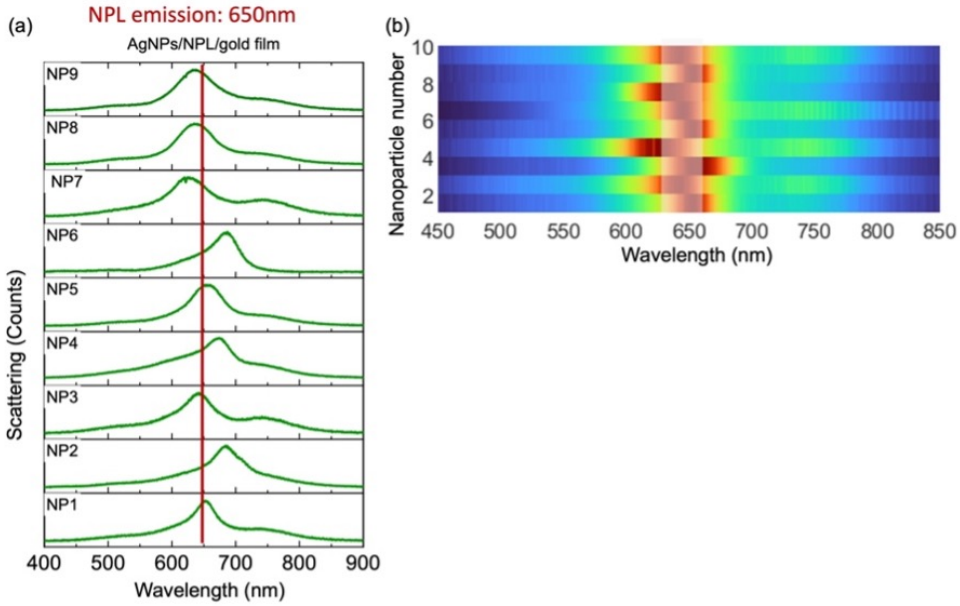

Figure S8: Dark field scattering data for different single particle NPoMs.

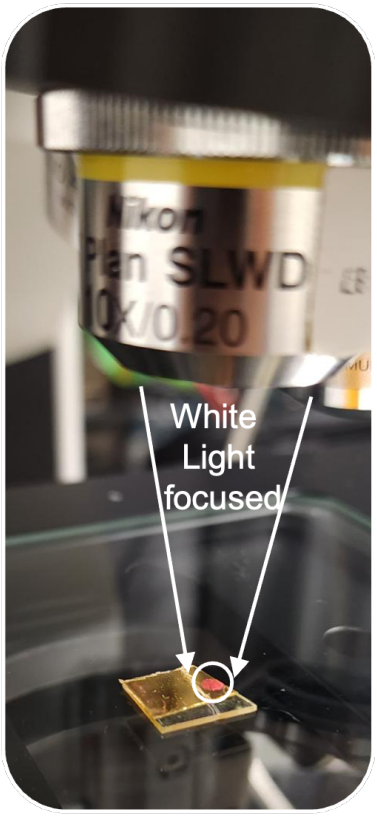

Figure S9: Setup up illustrating EF emission detection using white light excitation using naked eyes.

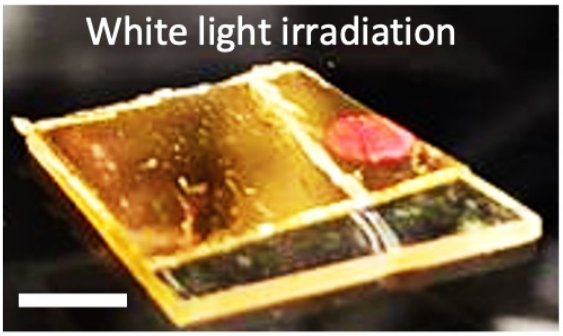

Figure S10: (a) Photograph showing EF in the form of distinct red emission spot observable by naked eye from densely arranged Ag NCs on top of a monolayer of NPLs, under illumination of white light Scale bar is 1 cm.

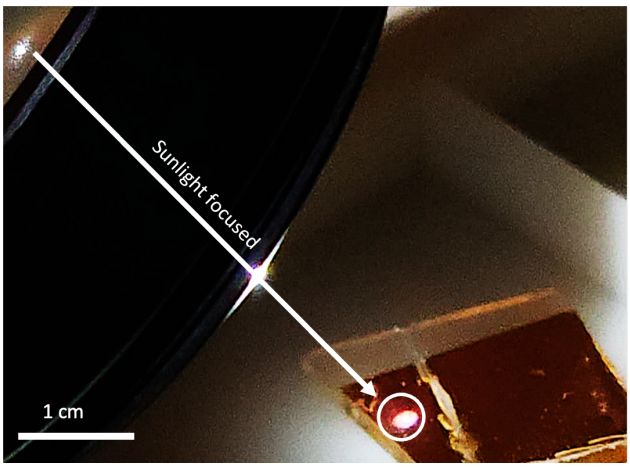

Figure S11: Setup up illustrating EF emission detection using sunlight excitation using naked eyes.

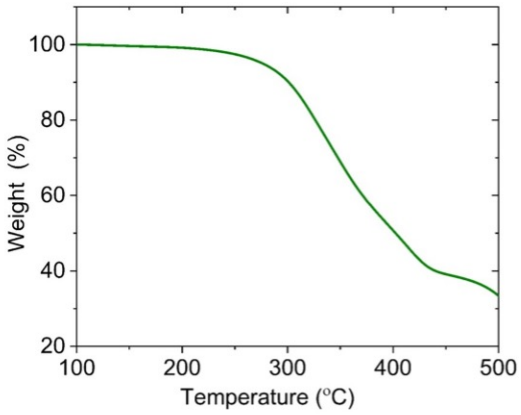

Figure S12: Thermogravimetric analysis of NPLs.

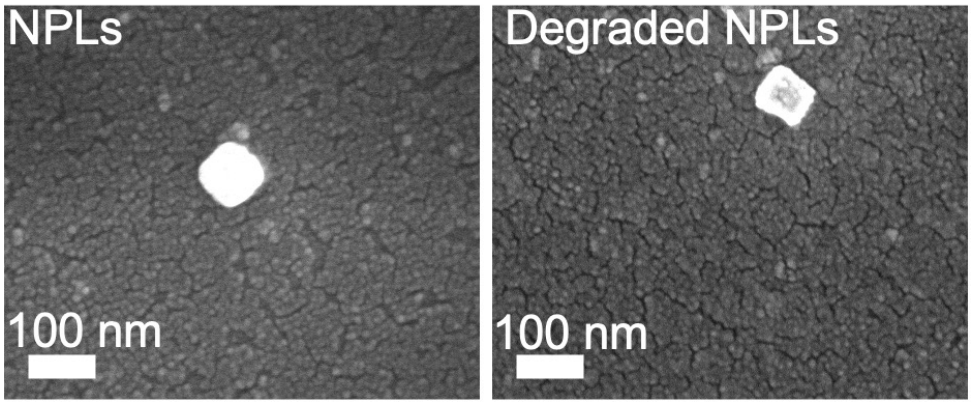

Figure S13: Scanning electron microscope (SEM) image of Left: NPLs, Right: Degraded NPLs.

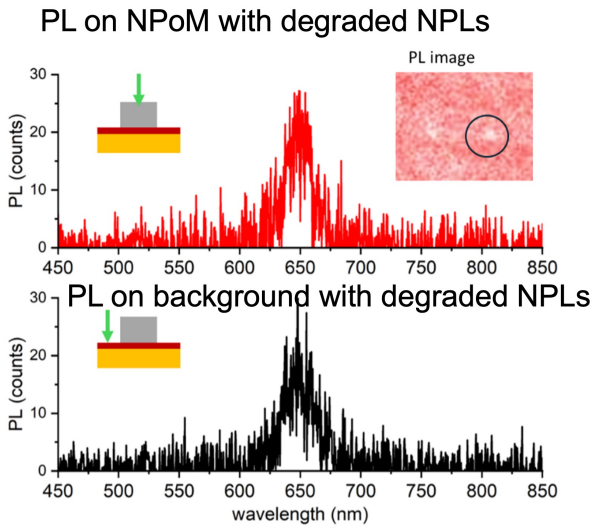

Figure S14: PL spectra observed from the NPoM structure with degraded monolayer of NPLs under laser excitation; Lower panel shows the PL spectra observed from the background with degraded monolayer of NPLs under laser excitation. The PL from the NPoM is nearly comparable to that of background showing that NPLs have been degraded throughout the sample.

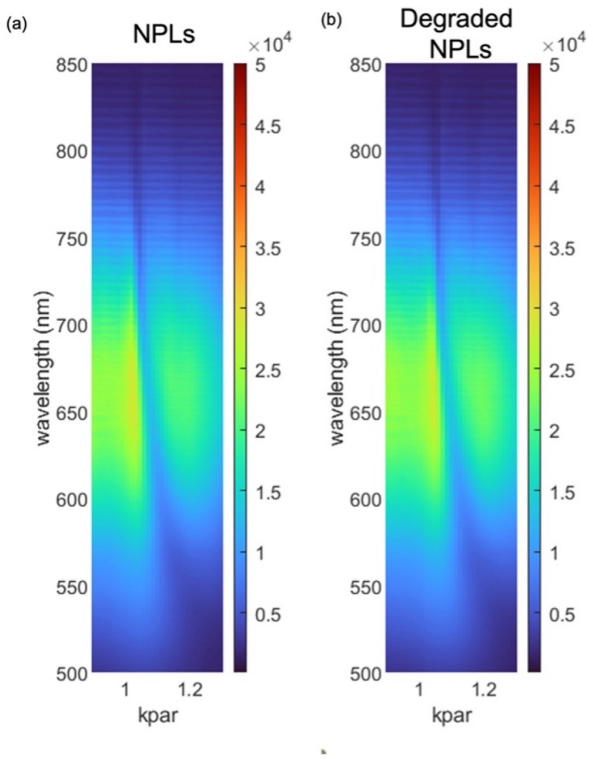

Figure S15: Comparison of the surface plasmon dispersion for (a) the emissive and the (b) the degraded NPL monolayer, both deposited on a 45 nm-thick silver film. Both plots appear identical indicating that the degraded NPLs exhibit similar optical properties as the as-deposited NPLs.

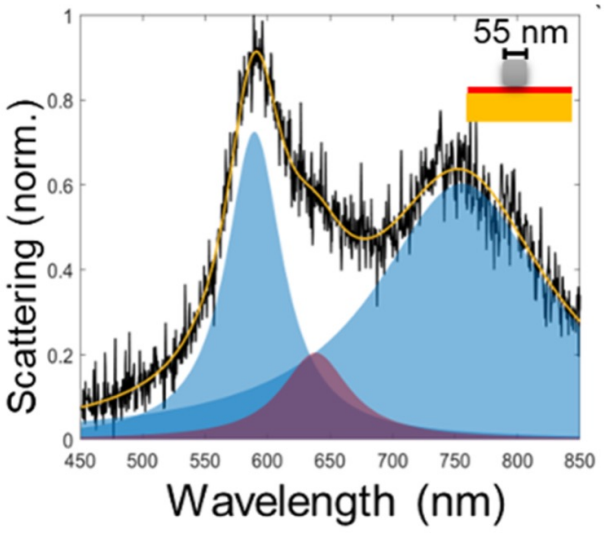

Figure S16: Dark-field scattering spectra for core shell red emitting CdSe/ CdZnS NPLs in NPoM cavity with smaller 55 nm Ag NC. Multiple peaks of the scattering spectrum are resolved and fitted to the Lorentz functions, showing three peaks at 575 nm, 650 nm, and 750 nm, respectively (filled blue and red curves).

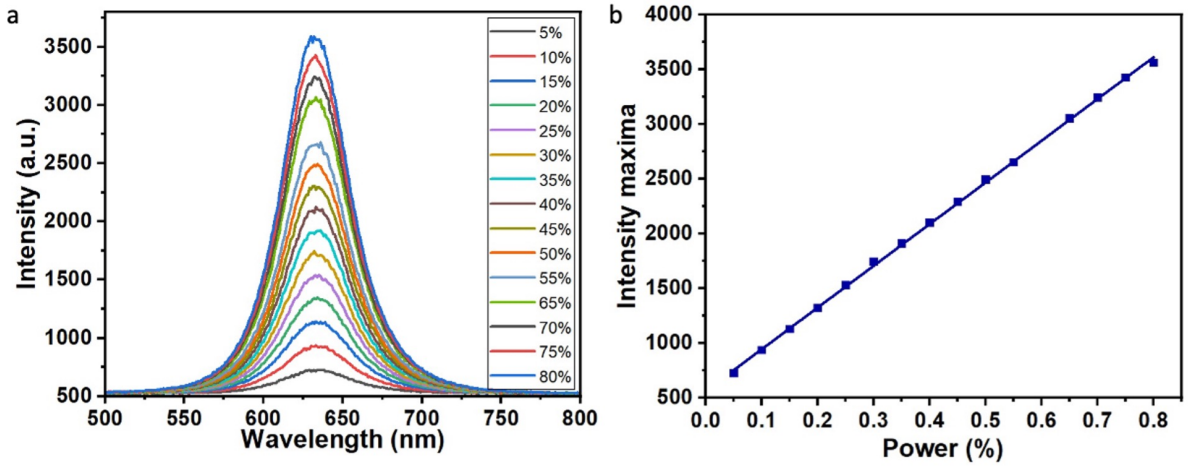

Figure S17: (a) PL spectra of CdSe/CdZnS core/shell NPLs spin-coated on a glass substrate under increasing laser excitation power (percentages indicated). (b) Intensity maxima versus laser excitation power for NPLs on glass, showing linear dependence.

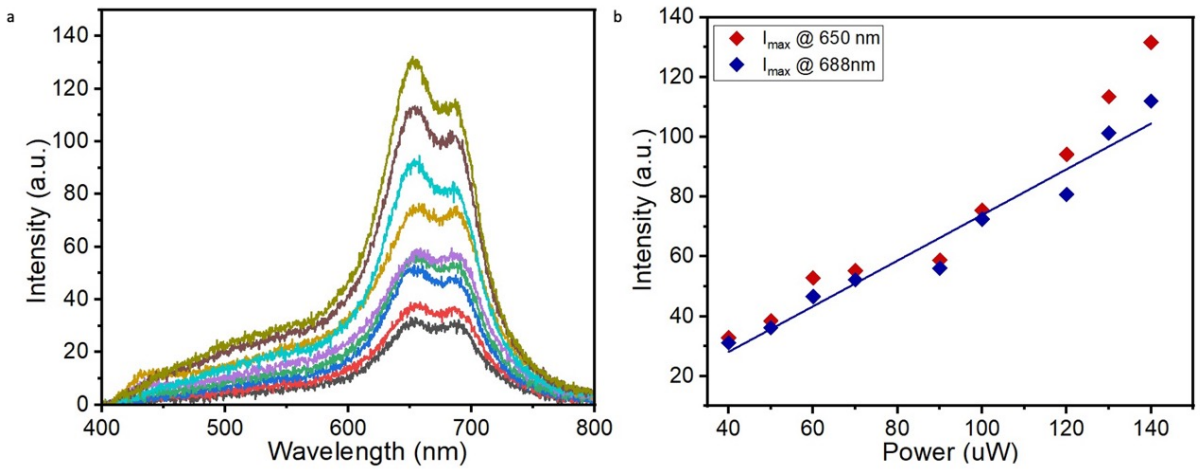

Figure S18: Dark-field scattering spectra with increasing power for core-shell CdSe/CdZnS red NPLs (b) Intensity maxima vs. pump power for 2 peaks at 650 nm and 690 nm.

Reference

1. Momper, R. *et al.* Kinetic control over self-assembly of semiconductor nanoplatelets. *Nano Letters* **20**, 4102–4110 (2020).

2. Erdem, O. *et al.* Orientation-controlled nonradiative energy transfer to colloidal nanoplatelets: engineering dipole orientation factor. *Nano Letters* **19**, 4297–4305 (2019).

3. Erdem, O. *et al.* Thickness-tunable self-assembled colloidal nanoplatelet films enable ultrathin optical gain media. *Nano Letters* **20**, 6459–6465 (2020).

4. Baruj, H. D. *et al.* Highly-directional, highly-efficient solution-processed light-emitting diodes of all-face-down oriented colloidal quantum well self-assembly. *Small* **19**, 2206582 (2023).

5. Wu, T. *et al.* Efficient hybrid method for the modal analysis of optical microcavities and nanoresonators. *J. Opt. Soc. Am. A* **38**, 1224–1231 (2021).

6. Esteban, R., Borisov, A. G., Nordlander, P. & Aizpurua, J. Bridging quantum and classical plasmonics with a quantum-corrected model. *Nat. Commun.* **3**, 825 (2012).

7. Garcia de Abajo, F. J. Nonlocal effects in the plasmons of strongly interacting nanoparticles, dimers, and waveguides. *J. Phys. Chem. C* **112**, 17983–17987 (2008).

8. Bai, Q., Perrin, M., Sauvan, C., Hugonin, J.-P. & Lalanne, P. Efficient and intuitive method for the analysis of light scattering by a resonant nanostructure. *Opt. Express* **21**, 27371–27382 (2013).

9. Wu, T., Arrivault, D., Yan, W. & Lalanne, P. Modal analysis of electromagnetic resonators: User guide for the man program. *Comput. Phys. Commun.* **284**, 108627 (2023).

10. Zhou, W.-j. *et al.* Probing spectral-hole-burning in non-hermitian scatterings: Differentiating far-field interference and near-field coupling. *ACS Photonics* **11**, 4671–4681 (2024).